

Boundary layer receptivity to free-stream sound on elliptic leading edges of flat plates

By JUAN B. V. WANDERLEY
AND THOMAS C. CORKE

University of Notre Dame, Aerospace and Mechanical Engineering Department,
Notre Dame, IN 46556, USA

(Received 7 January 1999 and in revised form 16 May 2000)

The leading-edge receptivity to acoustic waves of two-dimensional bodies is investigated using a spatial solution of the Navier–Stokes equations in vorticity/stream function form in general curvilinear coordinates. The free stream is composed of a uniform flow with a superposed periodic velocity fluctuation of small amplitude. The method follows that of Haddad & Corke (1998), in which the solution for the basic flow and the linearized perturbation flow are solved separately. The initial motivation for the work comes from past physical experiments for flat plates with elliptic leading edges, which indicated narrow frequency bands of higher neutral-curve Branch I receptivity. We investigate the same conditions in our simulations, as well as on a parabolic leading edge. The results document the importance of the leading edge, junction between the ellipse and flat plate, and pressure gradient to the receptivity coefficient at Branch I. Comparisons to the past experiments and other numerical simulations showed the influence of the elliptic leading-edge/flat-plate joint as an additional site of receptivity which, along with the leading edge, provides a wavelength selection mechanism which favours certain frequencies through linear superposition.

1. Introduction

Transition from laminar to turbulent flow in a boundary layer is of fundamental and practical importance, and as a result has been widely studied. Receptivity is the first stage of the transition process. The term receptivity was first used by Morkovin (1969) to describe the mechanism by which energy from the free stream enters and excites instability waves inside the boundary layer. In two-dimensional boundary layers, the linear instability is referred to as Tollmien–Schlichting (T-S) waves. For incompressible flows subject to free stream acoustic disturbances, the mechanism behind the receptivity process is one of a wavelength transformation between the long-wave acoustic disturbances and the shorter wavelength T-S modes. Goldstein (1983) was the first to point out that this process can take place in regions of strongly non-parallel mean flow. Such sites of receptivity include leading edges, and discontinuities in surface curvature, such as produced by local bumps or joints. General reviews on this topic have been made by Goldstein & Hultgren (1989), and Kerschen (1990).

Acoustic disturbances that enter the boundary layer by the receptivity process can excite different unsteady modes. These include a Stokes wave, forced (non-Orr–Sommerfeld) modes and T-S modes of both discrete and continuous spectrum types. These will grow or decay at different rates so that one may be more dominant

than another at a given downstream location. For leading-edge receptivity, the linear instability waves excited there are generally damped until they convect beyond the location of the lower neutral-growth curve (Branch I). Their amplitude at Branch I is dependent on the initial amplitude of the acoustic disturbance, the pressure gradient which governs the mean flow, and the frequency which determines the linear instability characteristics. If other sites of receptivity are present between the leading edge and Branch I, these will affect the instability amplitude measured at Branch I. Such observations make it essential to carefully define the receptivity coefficient.

In general, the receptivity coefficient is defined as the ratio of the instability wave (T-S) amplitude, at some location in the boundary layer, to the acoustic amplitude in the free stream. Leehey, Gedney & Her (1984) used the maximum amplitude in the boundary layer, which for a linear mode occurs at the location of the upper neutral-growth curve (Branch II). Murdock (1980), Saric, Wei & Rasmussen (1995), and Saric & White (1998) preferred to use the location of Branch I. Haddad & Corke (1998) advocated using the leading edge because this eliminated the other factors which influence the amplitude when measured downstream.

Historically, two basic body shapes have been used to study receptivity. Murdock (1980), Haddad & Corke (1998) and Hammerton & Kerschen (1992, 1996) considered parabolic bodies. In this case the only site of receptivity was at the leading edge, and the pressure gradient is everywhere favourable. In the first two references, the receptivity coefficient was determined by numerically solving the unsteady Navier–Stokes (N-S) equations. Hammerton & Kerschen (1992, 1996) determined it using asymptotic methods.

The other shape which has been frequently used is an elliptic leading edge on a finite-thickness flat plate. This shape has more practical relevance, and has been the subject of physical experiments by Shapiro (1977), Saric & Rasmussen (1992), Saric *et al.* (1995) and Saric & White (1998). The results of these motivated the N-S calculations of Lin, Reed & Saric (1990) and Fuciarelli (1997). The elliptic leading edge has an adverse pressure gradient, and two sites of receptivity, one at the leading edge and the other at the point where it joins the flat plate. To minimize the effect of the joint, Saric *et al.* (1995) used a ‘modified super ellipse’ (MSE). This used a variable exponent for the ellipse long axis to give zero curvature at the joint location.

Haddad & Corke (1998) and Hammerton & Kerschen (1992, 1996, 1997) found that the leading-edge receptivity coefficient increased as the leading-edge radius decreased, with the maximum receptivity occurring for an infinitely thin flat plate. When the receptivity values of Saric *et al.* (1995) and Fuciarelli (1997) were extrapolated upstream from Branch I to the leading edge, good quantitative agreement was found with the values of Haddad & Corke (1998).

Based on the analysis of Hammerton & Kerschen (1992, 1996), the receptivity coefficient determined at the leading edge varies with frequency through a Strouhal number based on the free-stream speed and nose radius. The dependence of the receptivity coefficient defined at Branch I on frequency will also reflect the frequency-dependent stability characteristics of the T-S waves. Linear theory predicts a smooth variation in the amplification rate so that the integrated (N-factor) amplitude should vary smoothly with frequency. A departure from this could occur when more than one site of receptivity exists at a streamwise location which is upstream of Branch I, for example at the leading edge and joint of the elliptic leading edge of a flat plate. In this case one can conceive of a mechanism of linear wave addition or cancellation which could produce unexpected amplitude variations with frequency.

This discussion leads to a series of experiments performed by Saric *et al.* (1995) and

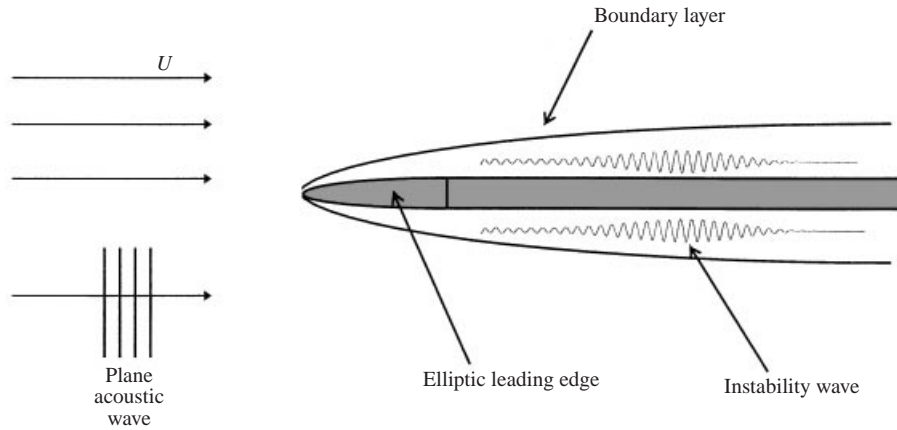


FIGURE 1. An illustration of the physical problem of interest.

Saric & White (1998). These examined the Branch I receptivity coefficient as a function of frequency for elliptic leading edges. The leading edges consisted of modified super ellipses (MSE) with aspect ratios of 20 : 1 and 40 : 1. In the first experiment, long-time-duration single-frequency acoustic disturbances were introduced inside the wind tunnel test section. The response to this excitation in terms of the T-S amplitude at Branch II was then measured, and used to infer the amplitude at Branch I based on linear stability theory growth rates. The receptivity coefficient was then defined as the T-S wave amplitude at Branch I divided by the acoustic wave amplitude. When they swept through different frequencies, they observed relatively narrow bands of frequencies in which the receptivity coefficient was larger. In addition, the interval of the bands was predictable based on wavelength arguments. Since that experiment, a number of possible explanations for this behaviour have been discussed: the formation of standing waves inside the tunnel test section, oblique angled sound waves which according to theory (Kerschen 1990; Hammerton & Kerschen 1996) have higher leading-edge receptivity, and nonlinear effects.

The explanation for this behaviour became the motivation for the second experiment, by Saric & White (1998). In this case, the sound source was excited with discrete frequencies in short-time-duration wave ‘packets’. The reason for this was the belief that the frequency bands observed in the earlier work were the result of an interaction between the wake instability of the flat plate and the leading-edge stagnation line. That is, the acoustic source was thought to excite the wake instability, which would produce an unsteady pressure oscillation at the leading edge, and thereby provide extra excitation to the T-S mode (see figure 1). The use of the acoustic wave packets was designed to utilize the slower convection speed of the T-S wave ($\simeq 0.4U_\infty$) compared to the acoustic-speed response of the plate-wake disturbance in order to separate out the two effects. The results of this experiment still revealed some frequency focusing of the Branch I receptivity, although the frequency width was larger.

1.1. Objectives

These experiments were a principle motivation for the present work, which also builds on the past work of Haddad (1995) and Haddad & Corke (1998). The objectives were then to numerically model the flow over elliptic leading edges matched to flat plates in order to directly compare to the results of the previous experiments by Saric *et al.* (1995) and Saric & White (1998). Here, the focus is on possible mechanisms that

could lead to the frequency focusing of higher Branch I receptivity. We selectively examine the roles of the leading edge, pressure gradient and junction on the receptivity coefficient determined at Branch I. For this, the effect of the junction is isolated by comparing a modified super ellipse and regular ellipse with the same aspect ratio and thickness.

We use the method of Haddad (1995) and Haddad & Corke (1998) whereby the basic and perturbation flows are solved separately in the spatial domain. In their cases for parabolic bodies, an analytic parabolic coordinate transformation was performed prior to the numerical formulation. For elliptic leading edges on flat plates, a formulation in general curvilinear coordinates is required.

We check the numerical model by first solving the flow over the parabolic body for the conditions of Haddad & Corke (1998). This is also checked against other available results in the literature, such as those of Davis (1972). We also check the numerical model for the elliptic leading edges against the available results in the literature, such as the experimental results of Saric *et al.* (1995), Saric & White (1998), and numerical results of Fuciarelli, Reed & Lyttle (1998). The comparisons include pressure gradients, the locations of Branch II, linear mode eigenfunctions, and the Branch I receptivity coefficients.

2. Governing equations

The acoustic receptivity of two-dimensional bodies in an incompressible flow was investigated by the numerical solution of the incompressible Navier–Stokes equations. By taking advantage of the two-dimensionality of the problem, the governing equations consist of two equations for the vorticity, ω , and stream-function, ψ , fields, and one equation for the pressure, p (or pressure coefficient, C_p), field. The non-dimensional form of the governing equations is

$$\omega_t + \psi_y \omega_x - \psi_x \omega_y = \frac{1}{R_L} (\omega_{xx} + \omega_{yy}), \quad (1a)$$

$$\omega = -\frac{1}{\sqrt{R_L}} (\psi_{xx} + \psi_{yy}), \quad (1b)$$

$$\nabla^2 C_p = 2[\psi_{xx} \psi_{yy} - (\psi_{xy})^2], \quad (1c)$$

where subscripts denote partial differentiation, and

$$R_L = \frac{U_\infty L}{\nu} \quad (2)$$

with L being a characteristic length which in this case is the length of the body.

The non-dimensional form of the governing equations has the advantage of showing explicitly the characteristic parameters of the flow such as Reynolds number. Moreover, the variables are normalized so that their values are restricted to certain limits such as 0 and 1. The form of non-dimensionalization which was used to obtain is (1)

$$x = \frac{x^*}{L}, \quad y = \frac{y^*}{L}, \quad t = \frac{t^* U_\infty}{L}, \quad \psi = \frac{\psi^*}{U_\infty L}, \quad \omega = \frac{\omega^*}{\sqrt{U_\infty^3 / \nu L}}, \quad C_p = \frac{p^* - p_\infty}{\rho U_\infty^2}. \quad (3)$$

The dimensionless governing equations were transformed from the physical Cartesian (x, y) coordinate into a general curvilinear coordinate (ξ, η) to make them more

suitable for a numerical formulation:

$$\mathbf{U}_\xi + \mathbf{V}_\eta = \mathbf{S} \quad (4)$$

where \mathbf{U} , \mathbf{V} and \mathbf{S} represent three different formulas corresponding to the respective equations 1(a)–1(c):

$$\mathbf{U} = \frac{1}{J} \begin{bmatrix} R_L^{-1}(A_1\omega_\xi + A_2\omega_\eta) \\ R_L^{-1/2}(A_1\psi_\xi + A_2\psi_\eta) \\ A_1C_{p_\xi} + A_2C_{p_\eta} \end{bmatrix}, \quad (5a)$$

$$\mathbf{V} = \frac{1}{J} \begin{bmatrix} R_L^{-1}(A_2\omega_\xi + A_3\omega_\eta) \\ R_L^{-1/2}(A_2\psi_\xi + A_3\psi_\eta) \\ A_2C_{p_\xi} + A_3C_{p_\eta} \end{bmatrix}, \quad (5b)$$

$$\mathbf{S} = \frac{1}{J} \begin{bmatrix} \omega_t + J(\psi_\eta\omega_\xi - \psi_\xi\omega_\eta) \\ -\omega \\ 2J^2[\psi_{\xi\xi}\psi_{\eta\eta} - (\psi_{\eta\xi})^2] \end{bmatrix}. \quad (5c)$$

The corresponding matrices and the Jacobian are collectively given as

$$A_1 = \xi_x^2 + \xi_y^2, \quad A_2 = \xi_x\eta_x - \xi_y\eta_y, \quad A_3 = \eta_x^2 + \eta_y^2, \quad J = \xi_x\eta_y - \xi_y\eta_x. \quad (6)$$

Equation (4) represents the three governing equations for vorticity, stream function and pressure in the general coordinates (ξ, η) . The equations for vorticity and streamfunction can be solved independently of the pressure. If only the pressure at the surface of the body is required, a simpler equation is obtained by applying the streamwise momentum equation to the fluid adjacent to the surface:

$$[C_{p_\xi}]_{wall} = -\frac{1}{\sqrt{R_L}}[\omega_\eta]_{wall}. \quad (7)$$

3. Perturbation of the governing equations

Following the method of Haddad & Corke (1998), the free stream is assumed to be composed of a uniform flow with a superposed uniform oscillation of frequency σ and amplitude ϵ . Here, ϵ is considered to be sufficiently small to allow linearization of the perturbation equations. In the curvilinear coordinates, the free-stream stream function is then expressed as

$$\psi_\infty = (1 + \epsilon e^{i\sigma t})\xi\eta. \quad (8)$$

The perturbation equations are obtained by linearizing the equations in §2 about the mean flow. The dependent variables are the superposition of the basic (mean) flow (Ψ and Ω) and the perturbation flow ($\tilde{\psi}$ and $\tilde{\omega}$) variables given in normal mode form as

$$\psi(\xi, \eta, t) = \Psi(\xi, \eta) + \epsilon e^{i\sigma t}\tilde{\psi}(\xi, \eta), \quad (9)$$

$$\omega(\xi, \eta, t) = \Omega(\xi, \eta) + \epsilon e^{i\sigma t}\tilde{\omega}(\xi, \eta). \quad (10)$$

Substituting these equations into the governing equations, and equating terms of equal powers of ϵ , leads to the governing equations for the basic and perturbation flow fields.

The basic flow (zero-order terms in ϵ) is governed by

$$\mathbf{U}_\xi + \mathbf{V}_\eta - \mathbf{S} = 0 \quad (11)$$

where in this case

$$\mathbf{U} = \frac{1}{J} \begin{bmatrix} -J\Omega\Psi_\eta + R_L^{-1}(A_1\Omega_\xi + A_2\Omega_\eta) \\ R_L^{-1/2}(A_1\Psi_\xi + A_2\Psi_\eta) \end{bmatrix}, \quad (12a)$$

$$\mathbf{V} = \frac{1}{J} \begin{bmatrix} J\Omega\Psi_\xi + R_L^{-1}(A_2\Omega_\xi + A_3\Omega_\eta) \\ R_L^{-1/2}(A_2\Psi_\xi + A_3\Psi_\eta) \end{bmatrix}, \quad (12b)$$

$$\mathbf{S} = \frac{1}{J} \begin{bmatrix} 0 \\ -\Omega \end{bmatrix}, \quad (12c)$$

and A_1 , A_2 , A_3 and J are the same as in (6).

The linearized perturbation flow (first-order terms in ϵ) is governed by

$$\mathbf{U}_\xi + \mathbf{V}_\eta = \mathbf{S} \quad (13)$$

where in this case

$$\mathbf{U} = \frac{1}{J} \begin{bmatrix} R_L^{-1}(A_1\tilde{\omega}_\xi + A_2\tilde{\omega}_\eta) \\ R_L^{-1/2}(A_1\tilde{\psi}_\xi + A_2\tilde{\psi}_\eta) \end{bmatrix}, \quad (14a)$$

$$\mathbf{V} = \frac{1}{J} \begin{bmatrix} R_L^{-1}(A_2\tilde{\omega}_\xi + A_3\tilde{\omega}_\eta) \\ R_L^{-1/2}(A_2\tilde{\psi}_\xi + A_3\tilde{\psi}_\eta) \end{bmatrix}, \quad (14b)$$

$$\mathbf{S} = \frac{1}{J} \begin{bmatrix} i\sigma\tilde{\omega} + J(\Omega_\xi\tilde{\psi}_\eta + \Psi_\eta\tilde{\omega}_\xi - \Omega_\eta\tilde{\psi}_\xi - \Psi_\xi\tilde{\omega}_\eta) \\ -\tilde{\omega} \end{bmatrix}, \quad (14c)$$

and again, A_1 , A_2 , A_3 and J are the same as in (6).

3.1. Boundary conditions

Basic flow On the surface of the body, the mean flow boundary conditions are the standard no-slip and no-penetration ones. In the curvilinear coordinate frame, these are specified by

$$\Psi = 0, \quad \Psi_\eta = 0, \quad \text{and} \quad \Omega = A_3\Psi_{\eta\eta}/\sqrt{R_L}. \quad (15)$$

Away from the body, in the free stream, the flow is uniform. This is given as

$$\Psi_\eta = \xi_x/J. \quad (16a)$$

Similarly, the free stream is vortex free so that

$$\Omega = 0. \quad (16b)$$

Perturbation flow On the surface of the body, the no-slip, no-penetration condition is specified by

$$\tilde{\psi} = 0, \quad \tilde{\psi}_\eta = 0, \quad \text{and} \quad \tilde{\omega} = A_3\tilde{\psi}_{\eta\eta}/\sqrt{R_L}. \quad (17)$$

Away from the body, in the free stream,

$$\tilde{\psi}_\eta = \xi_x/J \quad \text{and} \quad \tilde{\omega} = 0. \quad (18)$$

4. Numerical formulation

For the solution of the nonlinear basic flow equations, a pseudo-time marching, Beam–Warming (1978) implicit approximated factorization scheme was used. This scheme belongs to the class of alternating-direction implicit schemes (ADI), such as was used by Davis (1972) for the solution of the mean flow over parabolic bodies. In the numerical formulation, all the derivatives were approximated using a second-order finite differences. Away from the boundaries, central differencing was used.

On the body surface, the no-penetration condition was imposed by setting the stream function equal to zero. The no-slip condition was imposed implicitly in the computation of the vorticity given in (15). At the free-stream boundary, the free-stream condition was imposed by setting the undisturbed uniform velocity equal to one.

The method of defining the outflow boundary condition follows that of Haddad & Corke (1998). The properties at the outflow grid points are obtained together with the interior points by evaluating the streamwise derivatives of the convection terms with one-sided finite differences, and neglecting the streamwise elliptic terms of the governing equations. In order to avoid reflections that would alter the flow upstream, a buffer zone was specified in which the elliptic terms in the governing equations were multiplied by a weighting function, s , given by

$$s(i) = \left[\frac{1 + \tanh(\arg)}{2} \right] \quad \text{where} \quad \arg = 4 \left[1 - \frac{2(i - i_{buf})}{I_{max} - i_{buf}} \right]. \quad (19)$$

Here, i is the numerical index in the streamwise direction, i_{buf} is the index at the beginning of the buffer zone, and I_{max} is the total number of streamwise points. This weighting function ranges from 1 to 0, and thereby gradually suppresses the elliptic terms at the start of the buffer zone to the outflow boundary. The length of the buffer zone is an important parameter, and was set to be equal to four times the wavelength of the expected instability wave (Haddad & Corke 1998).

The linear equations governing the perturbation flow were solved by Gauss elimination using standard LINPACK routines. The boundary conditions on the surface were treated similarly to the mean flow. The outflow boundary condition was also handled like the basic flow using an identical buffer zone, with the weighting function given in (19).

The same computational grid was used for both the basic and perturbation flows. A stretching transformation was used in the streamwise ξ - and transverse η -directions in order to concentrate grid points close to the leading edge and surface of the body. With the stretching, care was taken to ensure that at least 10 grid points per instability wavelength would exist everywhere along the body.

The maximum height of the computational grid above the body surface corresponded to ten times the maximum thickness of the boundary layer, as recommended by Haddad (1995). The number of grid points in the ξ - and η -directions was 999 and 36, respectively.

The proper implementation of a numerical code was tested on parabolic bodies, where comparisons could be made to the published results of Davis (1972) and Haddad & Corke (1998), among others. In addition, that problem has the advantage of having an analytic (Blasius) solution in the limit as the nose radius of the parabola goes to zero (infinitely thin flat plate). The results of these tests showed excellent agreement both in terms of the mean flow, and instability mode amplitude and wavelength (see Wanderley 1998).

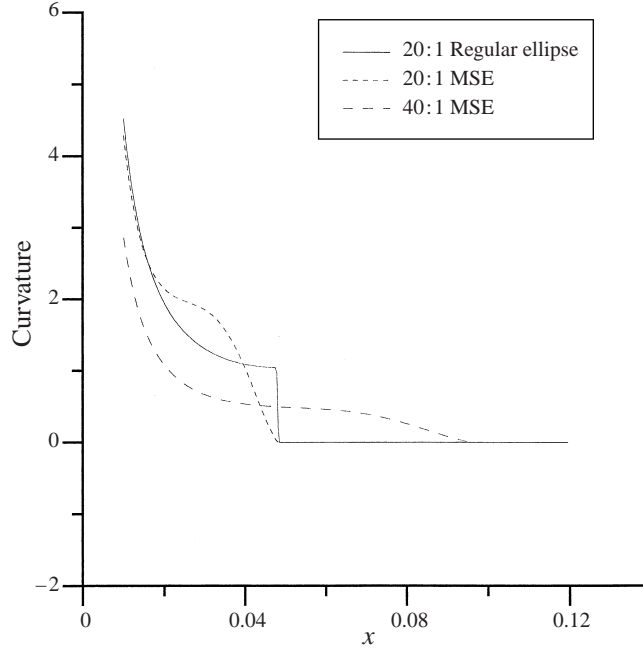


FIGURE 2. Curvature distributions for the three types of elliptic leading edges investigated.

Case	R_L	R_b	$F \times 10^6$	a/b
Present work 1	1.00×10^6	2400	30–120	20 : 1 MSE
Present work 2	1.00×10^6	2400	30–120	40 : 1 MSE
Present work 3	1.00×10^6	2400	30–120	20 : 1 Reg.E
Saric & White (1998)	1.90×10^6	2269	82–99	20 : 1 MSE
Fuciarelli <i>et al.</i> (1998)	—	2400	82–86	20 : 1 MSE

TABLE 1. Physical parameters with plate half-thickness, $b = 2.4 \times 10^{-3}$.

5. Results

As stated in §1.1, the focus of this work is on the acoustic receptivity of elliptic leading edges attached to finite-thickness flat plates. For this, three bodies were investigated: two modified super ellipses (MSE) with aspect ratios of 20 : 1 and 40 : 1, and one regular ellipse with an aspect ratio of 20 : 1. The first two were the subject of the experiments by Saric *et al.* (1995) and Saric & White (1998), which motivated our investigation. The comparison to a 20 : 1 regular ellipse is meant to isolate the effect of the junction to the flat plate over the other effects due to the leading edge and pressure gradient on the Branch I receptivity coefficient. The conditions of these three cases, as well as that of another numerical investigation by Fuciarelli *et al.* (1998), are listed in table 1.

The shape of the MSE is defined by

$$y = b \sqrt{1 - \left(\frac{a-x}{a}\right)^m} \quad \text{with} \quad m = 2 + \left(\frac{x}{a}\right)^2. \quad (20)$$

For a regular ellipse, $m = 2$.

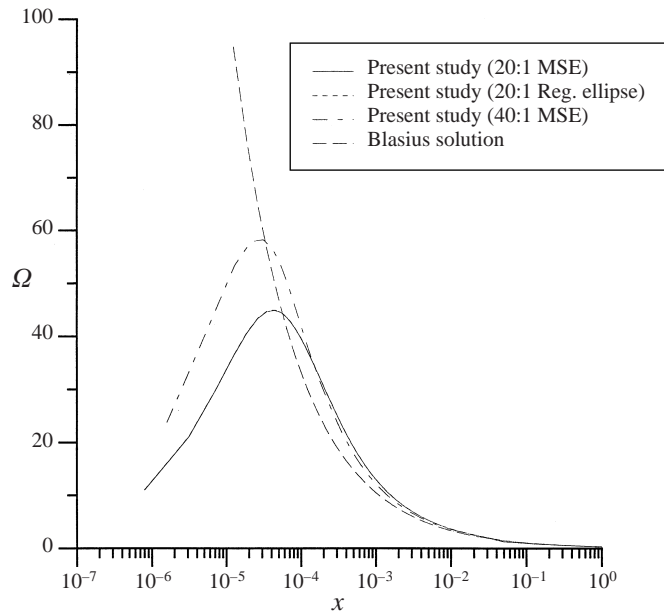


FIGURE 3. Surface vorticity distribution over flat plates with elliptic leading edges, and comparison to Blasius; $R_L = 1.00 \times 10^6$, and $R_b = 2400$.

With acoustic receptivity, as was first pointed out by Goldstein & Hultgren (1987), local changes in curvature are important. Figure 2 documents the curvature for the three leading edges examined in this study. The use of the MSE in the experiments was intended to give a zero curvature at the junction to the flat plate. Although the shape accomplishes this, it still exhibits a rapid variation just upstream of the junction.

5.1. Basic flow

The vorticity distribution on the surface of the three bodies is shown in figure 3. Also included is the vorticity distribution for a Blasius layer. We observe that distributions for the ellipses approach Blasius ones further downstream, away from the leading edge. Also, the vorticity level near the leading edge is larger for the higher (40 : 1) aspect ratio ellipse, which reflects its smaller leading-edge nose radius. Finally, we observe no difference between the vorticity distributions of the 20 : 1 MSE and regular ellipses.

The distribution of the surface pressure coefficient for the three bodies is shown in figure 4. These show a local region of adverse pressure gradient near the leading edge, which was not present for the parabolic body of Haddad & Corke (1998). The pressure distribution over the 40 : 1 MSE obtained in the experiment of Saric *et al.* (1995) is shown by the symbols in the figure. This shows a good agreement between the numerical and experimental results. In addition, both the 20 : 1 MSE and regular ellipses have nearly identical pressure distributions. This is important in trying to isolate the effect of the junction on the Branch I receptivity coefficient, which will be presented in the next section.

Other documentation of the mean flow presented by Wanderley (1998) included comparisons of the mean velocity profile over the flat-plate portion of the body with

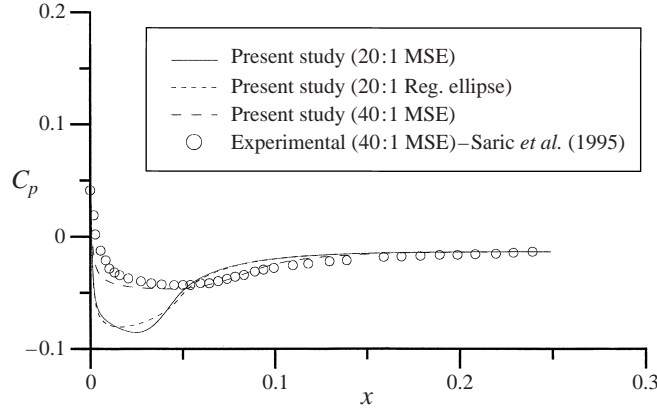


FIGURE 4. Surface pressure distribution over flat plates with elliptic leading edges, and comparison to Saric *et al.* (1995) for 20 : 1 MSE; $R_L = 1.00 \times 10^6$, and $R_b = 2400$.

different aspect-ratio leading edges. These showed excellent agreement with a Blasius profile.

5.2. Perturbation flow

In this section, the results of the investigation of the perturbation flow for the three leading edge cases are presented. For this a relatively large range and number of acoustic disturbance frequencies were examined. These totalled 180 different non-dimensional frequencies, $F = 2\pi f\nu/U_\infty^2$, in the range from 30×10^{-6} to 120×10^{-6} . This range of frequencies is illustrated with respect to the Blasius linear stability neutral curve by the pair of horizontal lines in figure 5. The length, s , used in $Re_s^{1/2}$ is the arclength along the body surface.

In presenting the perturbation flow, the contribution of the Stokes wave is always subtracted from the total perturbation velocity. This involved an independent solution of the governing equations which had been modified to eliminate the inertial terms. The numerical accuracy had been tested by comparing to the analytic Stokes solution. The details of this are presented by Wanderley (1998).

Figure 6 shows the wall-normal distribution of the streamwise velocity perturbation amplitude at the streamwise location of Branch II of the neutral curve, for the 20 : 1 MSE leading edge at $R_L = 1.44 \times 10^6$, $b = 1.67 \times 10^{-3}$ and $R_b = 2400$. Note that in this case, the conditions are different from those given in table 1 to allow a direct comparison to the experimental results of Saric *et al.* (1995). These are shown as the open symbols in the figure. Also shown by filled symbols is the linear theory T-S eigenfunction. Both the numerical and experimental results were obtained for a non-dimensional frequency of $F = 54 \times 10^{-6}$. With this comparison, we observe good agreement between linear theory and the present numerical results. The experimental results also compare very well except for a small deviation near the edge of the boundary layer.

A further comparison between our numerical results, linear theory and the experimental results is shown in figure 7. This shows the Reynolds number value at the upper branch (II) of the neutral stability curve for a range of frequencies of $35 \times 10^{-6} \leq F \leq 60 \times 10^{-6}$. These were for a 20 : 1 MSE leading edge with a thickness of $b = 5.0 \times 10^{-3}$ and $R_b = 20\,000$, to match other experimental conditions of Saric *et al.* (1995). The results of the experiment are shown by the closed symbols. The open

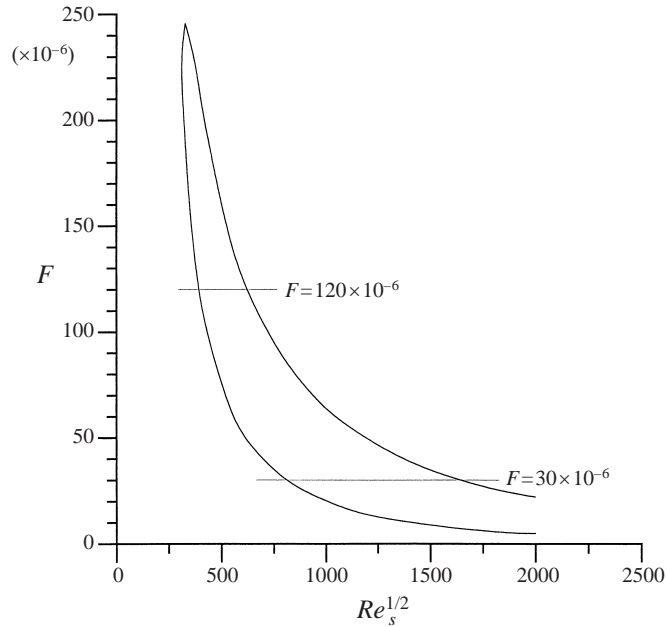


FIGURE 5. Neutral stability curve for the Blasius boundary layer showing the range of dimensionless frequencies used for the parabola and elliptic leading edges.

symbols in the figure correspond to the linear theory predictions for a Blasius layer. Here we find good agreement between the experimental and the numerical results. It might be expected that both of these would differ from the linear theory prediction since the flow only approaches Blasius far from the leading edge. Since the location of Branch II is one of the most sensitive indicators of the stability characteristics of the basic flow, the close correspondence of our numerical results with the experiment is significant.

Figure 8 shows representative amplitude distributions in the streamwise direction of the perturbation velocity for the three bodies at $F = 80.0 \times 10^{-6}$. These correspond to the height above the wall where the T-S amplitude is near a maximum. The long vertical lines denote the amplification region in each case. The junction between the ellipse and the flat plate in each case is denoted by the short vertical line near the x -axis of each plot.

We define the receptivity as the ratio of the maximum T-S amplitude at an x -location, to the amplitude of the free-stream disturbance, which is denoted as $K_x = |(u'_{TS})|/|(u'_{\infty})|$. One of the advantages of this definition is that an explicit amplitude for the free-stream disturbance is not required. Rather, we only require that the free-stream amplitude be small enough for linearization. In our formulation, the amplitude obtained from the numerical results is u'/u'_{∞} . Therefore if the only component of the fluctuations is due to T-S waves, the amplitude we measure is u'_{TS}/u'_{∞} and so the amplitudes measured at any x -location such as in the plots in figure 8, are identically K_x . For comparison to the results of Saric *et al.* (1995), and Saric & White (1998), we chose x to be at the locations of Branch I so that we report K_I .

Figure 9 shows the effect of the different frequencies on K_I for the three different elliptic leading edges, at the conditions given in table 1. The points in the figure

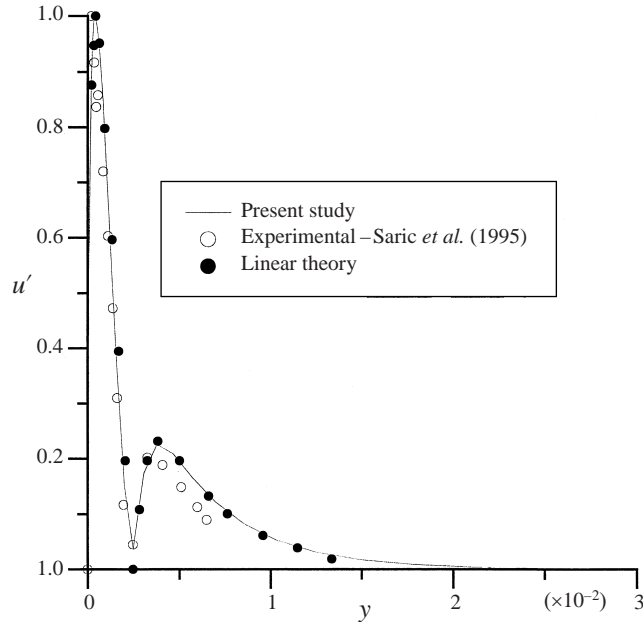


FIGURE 6. Wall-normal distribution of the streamwise velocity amplitude of the instability wave at Branch II over a flat plate with a 20 : 1 MSE leading edge, and comparison to the experimental results of Saric *et al.* (1995), and linear T-S eigenfunction; $R_L = 1.44 \times 10^6$, $F = 54 \times 10^{-6}$, $R_b = 2400$.

correspond to the values at discrete frequencies. Note that these represent every sixth frequency increment. In subsequent figures these will be represented by the smooth curve which is drawn through the points in this figure.

We can observe a number of features about the receptivity coefficients in figure 9. The first is that there is an oscillation in the receptivity coefficient with changing disturbance frequency. This is most evident for the 20 : 1 regular ellipse and the 40 : 1 MSE. The period of the oscillation is also shorter for the larger-aspect-ratio leading edge. The longer period of oscillation for the shorter-aspect-ratio cases, and a downstream shift in the location of the maxima did not allow us to capture the period minima which is expected for the 20 : 1 MSE within the frequency range examined. In addition to these interesting observations, we also find that the largest receptivity coefficient occurs for the lower-aspect-ratio leading edges. This might appear to conflict with the previous results of Haddad & Corke (1998) and Hammerton & Kerschen (1992) which indicate that the smaller nose radius of the 40 : 1 MSE should have the highest (leading edge) receptivity. In subsequent figures we will examine these features and give a physical explanation for this behaviour.

As discussed earlier, with these bodies the amplitude of the T-S waves at Branch I is dependent on the receptivity at the leading edge and at the junction with the flat plate, and on the pressure gradient which defines the mean flow near the leading edge. Figure 10 documents the leading-edge receptivity, K_{LE} , for the three cases. This shows the T-S amplitude on a log scale, as a function of x -location close to the leading edge. The amplitude at the leading edge ($x = 0$) is expected to decay exponentially until reaching Branch I. On a log scale this should follow a straight line. Following the method of Haddad & Corke (1998), a straight line was fitted to the points closest to the leading edge in order to extrapolate to the values at $x = 0$. The result shows that as expected, K_{LE} is larger for the sharper, 40 : 1 leading edge. The value also

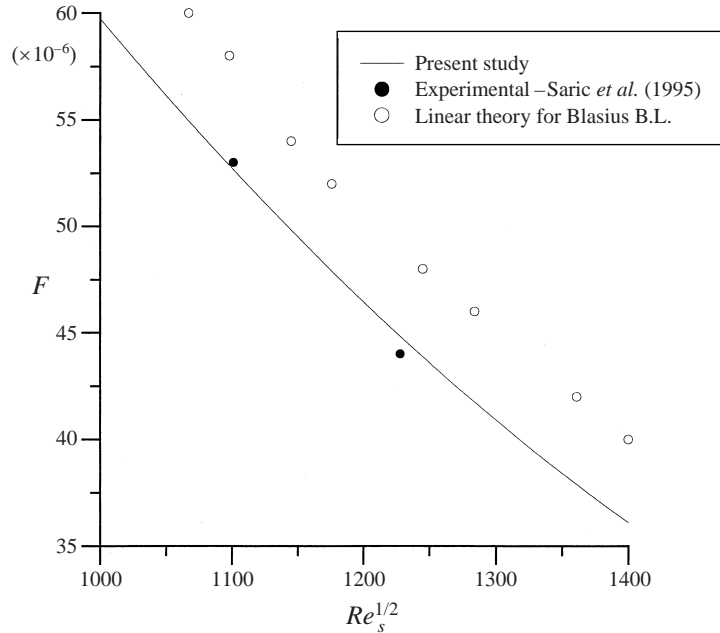


FIGURE 7. Upper branch of the neutral growth curve for a flat plate with a 20 : 1 MSE leading edge, and comparison to the experimental results of Saric *et al.* (1995), and linear theory for a Blasius layer.

compares well to $K_{LE} = 0.6$ that was obtained for the parabola with a comparable nose-radius Strouhal number by Haddad & Corke (1998). It should be pointed out that the higher frequency of $F = 230 \times 10^{-6}$ used by Haddad & Corke (1998), makes their extrapolation for K_{LE} less accurate than in the present results (see Erturk & Corke 2000).

The two 20 : 1 ellipses have the same nose radius and therefore are expected to have the same value of K_{LE} . This in fact was the case, within the accuracy of the extrapolation, as seen in figure 10. In figure 9, the maximum value of K_I is slightly larger for the regular ellipse than for the MSE. The reason for this is the slight differences in the pressure gradient in these two cases. As a result, even though the instability amplitude started at the same level, it decayed faster for the MSE giving a lower value at Branch I. The 40 : 1 MSE had the highest amplitude at the leading edge, but it also had the smallest adverse pressure gradient of the three cases. As a result, its decay rate was even faster than the others which accounts, in part, for the lowest values of K_I .

The origin of the oscillation, and the period of the receptivity can be traced to an interaction between instability waves which originate at the two sites of receptivity. This is illustrated in the schematic at the top part of figure 11. The bottom part of the figure corresponds to the Branch I receptivity coefficients for the 40 : 1 MSE. As shown, instability waves convect downstream from the leading edge and junction to the measurement location at Branch I. At a given frequency, the wavelength of the waves originating at the two sites is the same. We also expect these waves to have the same initial phase difference with respect to the free-stream acoustic disturbance. As such, when there is an integer number of wavelengths between the leading edge and junction, the waves will be in phase and their amplitudes will add. When there

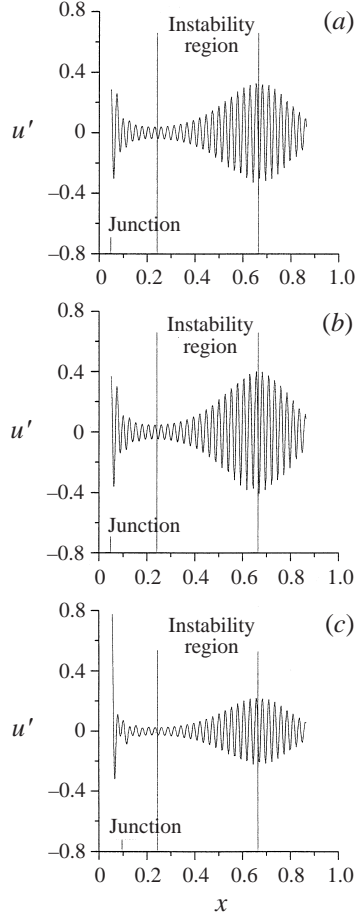


FIGURE 8. Streamwise perturbation amplitude distribution in the streamwise direction at a fixed height above the surface after subtracting the Stokes wave: (a) 20 : 1 MSE, (b) 20 : 1 regular ellipse, (c) 40 : 1 MSE; $R_L = 1.00 \times 10^6$, $F = 80.0 \times 10^{-6}$, $R_b = 2400$.

is an integer plus one-half number of wavelengths between the leading edge and junction, there will be a 180° phase shift between the two waves and the amplitudes will subtract.

In figure 11, we defined the distance from the leading edge to the junction as a . From the numerical results for the 40 : 1 MSE, we determined the streamwise wavelengths of the T-S waves at the frequencies where the local maxima and minima in the receptivity were found to occur. These are marked at their respective locations on the plot. There, λ_1 and λ_3 refer to minima, and λ_2 and λ_4 refer to maxima. We then determined the number of wavelengths at these frequencies which correspond to a . The result supports the linear superposition model, namely

$$a = 2.5\lambda_1 = 3.0\lambda_2 = 3.5\lambda_3 = 4.0\lambda_4. \quad (21)$$

In this light, we next consider the 20 : 1 ellipses, for which the Branch I receptivity coefficients as a function of frequency have been re-plotted in figure 12. We first focus on the MSE. This case has a high, well-defined maximum. At this point the T-S wavelength λ_3 was found to be 0.0240. Putting this in terms of the distance between

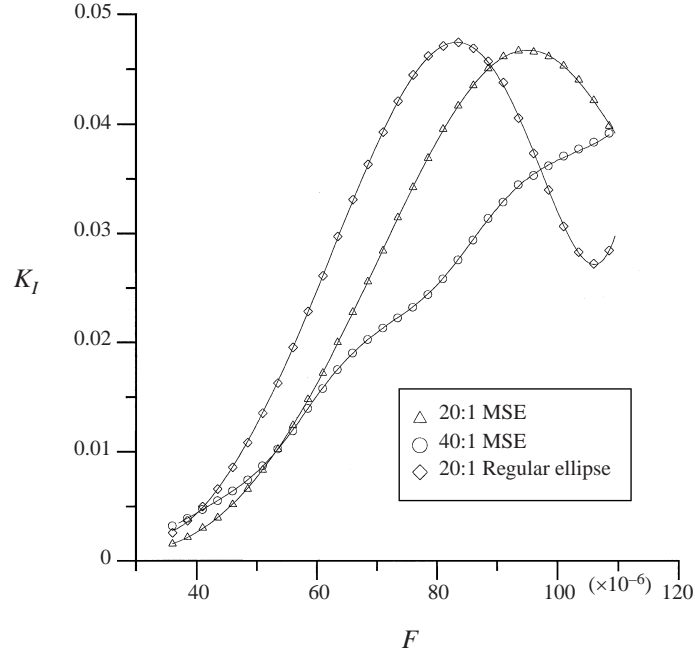


FIGURE 9. Receptivity coefficients at Branch I as a function of frequency over flat plates with elliptic leading edges; $R_L = 1.00 \times 10^6$, $R_b = 2400$.

the leading edge and junction, $a = 2\lambda_3$. This again supports the linear superposition model to explain the local maximum in the K_I at this frequency.

Finally we consider the 20 : 1 regular ellipse. In this case, there are well-defined local maximum and minimum which appear in the K_I distribution. After determining the wavelengths at these two frequencies, the relation between those and the distance between the leading edge and junction is found to be $2\lambda_1 = 2.5\lambda_2 = 1.11a$. Although this is not as good as the other two cases, we feel that it still supports the linear superposition model for the Branch I receptivity variation with frequency. There is also another explanation which will be considered shortly.

Further evidence of the linear superposition model comes from considering the difference in the period of oscillation of K_I with frequency between the cases. With these, the distance between the leading edge and junction for the 40 : 1 MSE is twice that of the 20 : 1 MSE. Therefore we expect twice as many instability wavelengths corresponding to a for the 40 : 1 MSE. This is evident by comparing the number of wavelengths corresponding to a at the frequency where the local maximum exists in the two cases ($F \simeq 96 \times 10^{-6}$). In this comparison, $a = 2\lambda$ for the 20 : 1 MSE, and $a = 4\lambda$ for the 40 : 1 MSE.

The instability wavelength is $\lambda = C_r/2\pi f$, where the phase speed, C_r , is a function of frequency. Therefore, $\lambda \propto f^{-k}$, where k is a positive number. Figure 13 shows this relation, which is independent of the three leading-edge cases. With twice the number of wavelengths corresponding to a for the 40 : 1 MSE, we expect that the change in the phase between the waves generated at the leading edge and those generated at the junction will be twice as fast as that for the 20 : 1 MSE. Therefore the occurrence of a 0° phase difference, producing a local K_I maximum, or 180° phase difference, producing a local minimum, will vary twice as fast with frequency for the 40 : 1

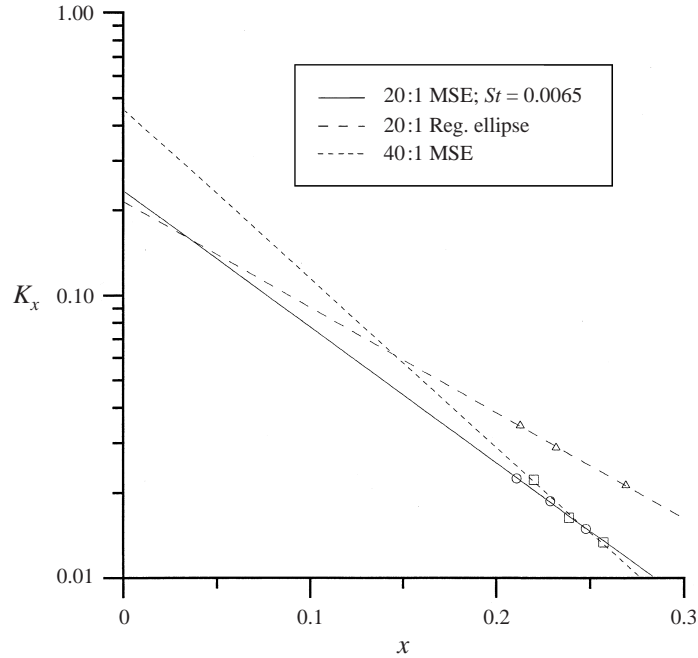


FIGURE 10. Receptivity coefficients near the leading edge used to extrapolate to leading-edge coefficient for flat plates with elliptic leading edges; $R_L = 1.00 \times 10^6$, $F = 54.0 \times 10^{-6}$, $R_b = 2400$.

compared to the 20 : 1 aspect ratio. This in fact is what we observe by comparing figures 11 and 12.

The comparison between the 20 : 1 regular ellipse and MSE was intended to isolate the effect of the junction. To a certain degree it did. These two cases had the same leading-edge radius, and thereby the same leading-edge receptivity coefficient, as demonstrated in figure 10. We did however observe a small difference in the pressure gradient, which might be expected to produce a small difference in the basic flow. This however had a minimum effect on the instability wavelength at a given frequency, as was documented in figure 13, where it was not affected by the aspect ratio or shape of the elliptic leading edge. This also agrees with the experimental results of Saric *et al.* (1995).

The most important difference we observe between the two 20 : 1 elliptic leading edges is that the period of oscillation of K_I is shorter for the regular ellipse. This would suggest that there was a slight phase lag in the waves produced at the junction of the regular ellipse. Specifically the phase lag would correspond to 0.11λ , or approximately 40° . Another way to think of this is as an ‘effective’ receptivity site which is located slightly further downstream of the physical junction. In this case it would be located at $x = 0.0533$ compared to 0.050.

Finally, with regard to our original motivation, we make a quantitative comparison between the present results for the 20 : 1 MSE and the experiments of Saric *et al.* (1995), and Saric & White (1998), and the numerical results of Fuciarelli *et al.* (1998). This is done in figure 14 which shows the Branch I receptivity coefficient as a function of frequency. At frequencies which are representative of all the studies, $F \times 10^6 = 82 - 92$, the agreement in the receptivity coefficient is reasonably good. This is summarized in table 2.

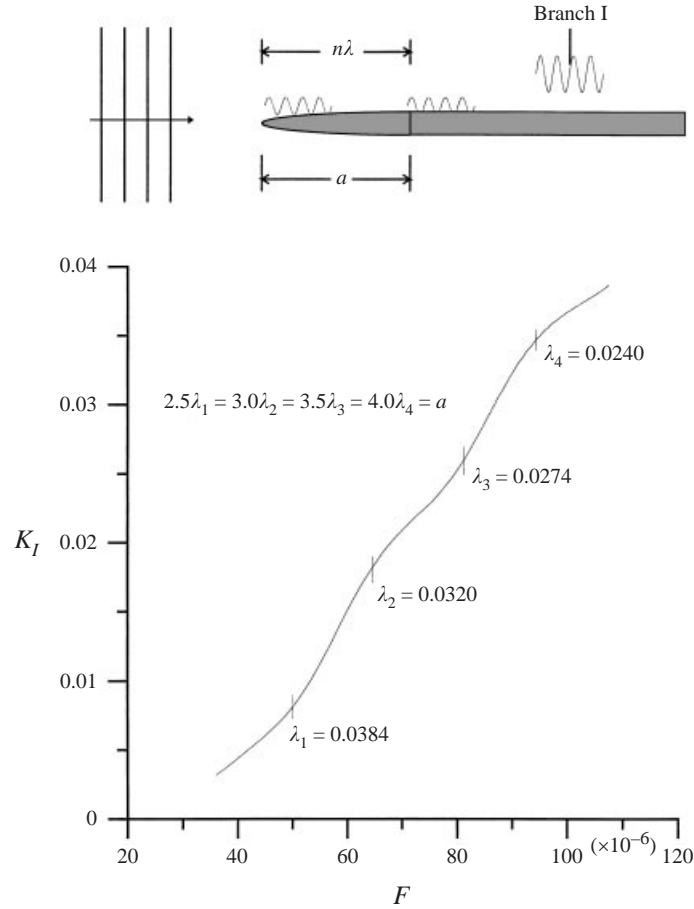


FIGURE 11. Receptivity coefficient at Branch I as a function of frequency over a flat plate with a 40 : 1 MSE leading edge showing the relation between local maxima and minima and the number of instability wavelengths between the two points of receptivity; $R_L = 1.00 \times 10^6$, $R_b = 2400$.

Case	Present work	Fuciarelli <i>et al.</i> (1998)	Saric <i>et al.</i> (1995)	Saric & White (1998)
$F \times 10^6$	90	82–86	84	88–92
K_I	0.046	0.048	0.036	0.050 ± 0.005

TABLE 2. Branch I receptivity coefficients for the 20 : 1 MSE, $R_b = 2400$.

The present numerical results show a variation of K_I with frequency which is broader than in the experiments. It is interesting however that although the receptivity values in the experiment fall in narrower bands, the peak levels approximate the variation with frequency that was found in the present study. As discussed in the Introduction, physical experiments on acoustic receptivity are extremely difficult to perform. The amplitudes are small, and there are a number of competing effects which can control the outcome. Therefore the agreement that is observed in table 2 is more of a testament to the quality of the experiments than to the numerical

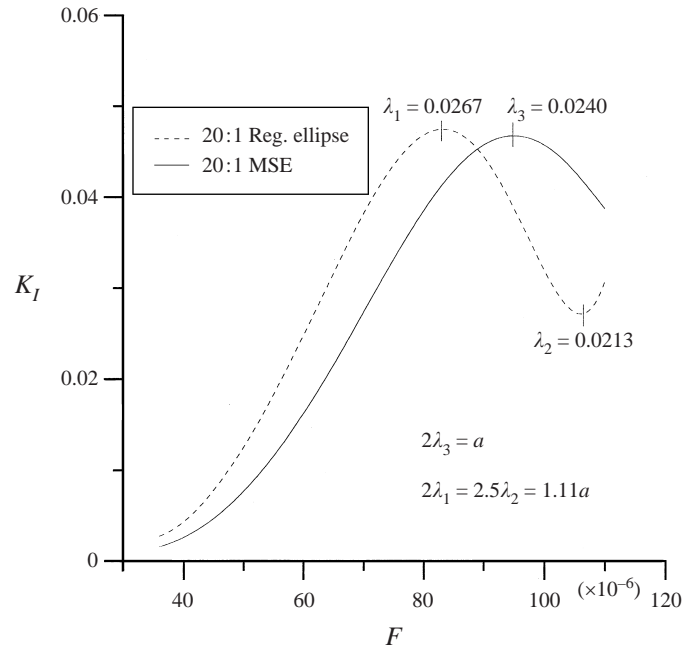


FIGURE 12. Receptivity coefficient at Branch I as a function of frequency over a flat plate with 20 : 1 MSE and regular ellipse leading edges showing the relation between local maxima and minima and the number of instability wavelengths between the two points of receptivity; $R_L = 1.00 \times 10^6$, $R_b = 2400$.

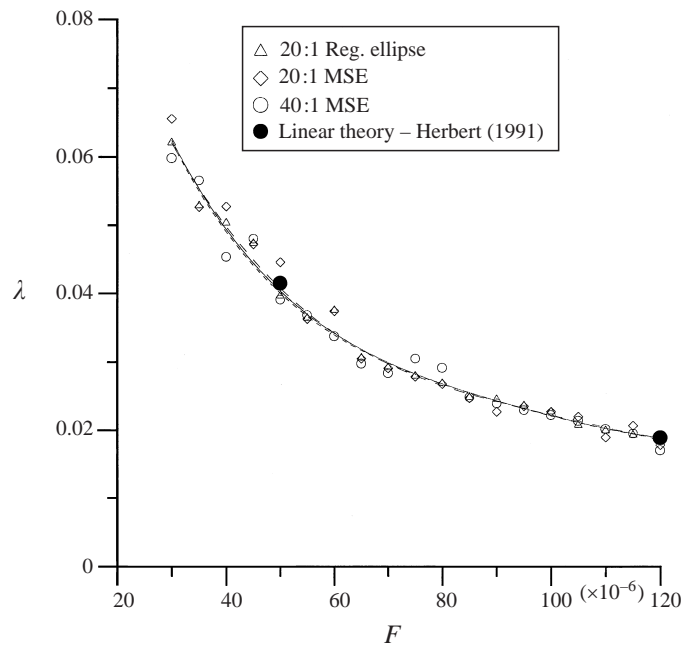


FIGURE 13. Wavelength of the instability wave over flat plates with elliptic leading edges measured at Branch I, and comparison to linear theory; $R_L = 1.00 \times 10^6$, $R_b = 2400$.

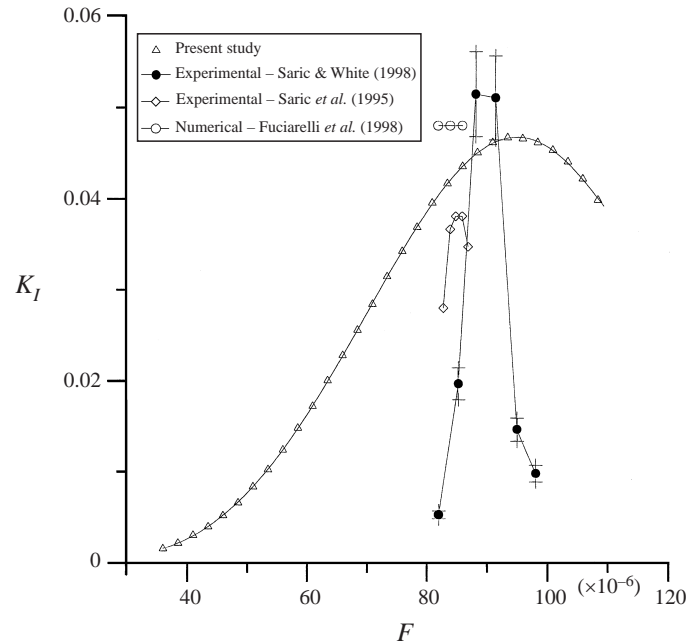


FIGURE 14. Receptivity coefficient at Branch I as a function of frequency over a flat plate with a 20 : 1 MSE leading edge, and comparison to the experimental results of Saric *et al.* (1995), Saric & White (1998), and Fuciarelli *et al.* (1998); $R_b = 2400$.

simulation. Clearly these calculations were motivated by the experiments. However, in this problem, it may be that the only way to get the complete physics is through the combination of experiments and numerical simulations such as this, and by others.

6. Conclusions

The spatial approach to study the receptivity to acoustic disturbances of boundary layers previously used for parabolic bodies by Haddad & Corke (1998) was successfully adapted to study finite-thickness flat plates with elliptic leading edges. This used a formulation in general curvilinear coordinates which will allow the study of other body shapes in the future.

This work was motivated by the experiments of Saric *et al.* (1995), and Saric & White (1998), so that their conditions were simulated. This consisted of 40 : 1 and 20 : 1 aspect-ratio modified-super-ellipse leading edges on flat plates at a Reynolds number based on the plate thickness of $R_b = 2400$. In order to attempt to separate out the effect of the leading edge and pressure gradient on the Branch I receptivity, a 20 : 1 regular ellipse at the same conditions was also studied.

The numerical code was tested with the parabolic bodies used by Haddad & Corke (1998) and excellent agreement was found in terms of the basic and perturbation flows. For the elliptic leading edges, we found excellent agreement with the experimental results of Saric *et al.* (1995) in terms of the surface pressure coefficient, wall-normal eigenfunction of the streamwise perturbation velocity, and locations of the upper branch of the neutral growth curve.

When we focused on the leading edge, we found that the 40 : 1 MSE had the largest leading-edge receptivity coefficient. This agreed with Haddad & Corke (1998)

and Hammerton & Kerschen (1992), who showed that the leading-edge receptivity increases as the nose radius decreases. The value obtained for the 40 : 1 MSE was also close to that obtained for the parabolic body at the same nose-radius Strouhal number. As an additional check, we found that the leading-edge receptivity coefficient for the two 20 : 1 elliptic leading edges (with the same nose radius) agreed as required by theory.

Although the 40 : 1 MSE had the largest leading-edge receptivity coefficient, its receptivity coefficient at Branch I was the lowest of the three. This was the result of having a smaller adverse pressure gradient which increased the decay rate of the instability mode. The pressure gradients for the two 20 : 1 ellipses were nearly identical, and the maximum Branch I receptivity coefficients in the two cases were also nearly the same.

Unlike the parabolic body, the flat plates with elliptic leading edges have two sites of Branch I receptivity. These are the leading edge, as before, and the junction between the elliptic leading edge and flat plate. The junction was found to be active in all three cases. This led to a periodic increase and decrease in the Branch I receptivity coefficient with acoustic excitation frequency. This behaviour was traced to the linear addition and subtraction of waves which originated from the two receptivity sites. Local receptivity maxima occurred at frequencies which gave an integer number of wavelengths (0° phase shift) between the leading edge and joint. Local minima occurred when an integer number plus one-half wavelengths (180° phase shift) occurred between the leading edge and joint. This was also consistent with the observation that receptivity maxima and minima varied twice as fast with frequency for the 40 : 1 MSE compared to the 20 : 1 MSE.

The variation of the instability wavelength with frequency was the same for all three leading edges. This agreed with the experiments of Saric *et al.* (1995), and the linear stability calculations of Herbert (1991).

Finally, for the 20 : 1 MSE within a band of frequencies, $F \times 10^6 = 82-92$, very good quantitative agreement was found for the Branch I receptivity coefficient between the present results, the experiment of Saric & White (1998), and the numerical results of Fuciarelli *et al.* (1998). These were 0.046, 0.050 ± 0.005 , and 0.048, respectively. However, over the full band of frequencies examined in our study ($30 \leq F \times 10^6 \leq 120$) the coefficient variation with frequency is broader than depicted by the experiment. Therefore other unknown effects, which are not a part of the numerical simulation, are in play in the experiments.

The authors have benefited from discussions on this work with Professors William Saric and Helen Reed. Their interest and help has been very much appreciated.

REFERENCES

- BEAM, R. M. & WARMING, R. F. 1978 An implicit factored scheme for the compressible Navier–Stokes equations. *AIAA J.* **16**, 393–402.
- DAVIS, R. T. 1972 Numerical solution of the Navier–Stokes equations for symmetric laminar incompressible flow past a parabola. *J. Fluid Mech.* **51**, 417–433.
- ERTURK, E. & CORKE, T. C. 2000 Boundary layer leading edge receptivity to sound at incident angles. *J. Fluid Mech.* (submitted).
- FUCIARELLI, D. A. 1997 Numerical simulation of leading edge receptivity. PhD thesis, Arizona State University.
- FUCIARELLI, D. A., REED, H. L. & LYTTLE, I. 1998 DNS of leading-edge receptivity to sound. *AIAA Paper* 98-2644.

- GOLDSTEIN, M. E. 1983 The evolution of Tollmien–Schlichting waves near a leading edge. *J. Fluid Mech.* **127**, 59–81.
- GOLDSTEIN, M. E. & HULTGREN, L. S. 1989 Boundary-layer receptivity to long-wave free-stream disturbances. *Ann. Rev. Fluid Mech.* **21**, 137–166.
- HADDAD, O. M. 1995 Numerical study of leading edge receptivity over parabolic bodies. PhD thesis, Illinois Institute of Technology.
- HADDAD, O. M. & CORKE, T. C. 1998 Boundary layer receptivity to free-stream sound on parabolic bodies. *J. Fluid Mech.* **368**, 1–26.
- HAMMERTON, P. W. & KERSCHEN, E. J. 1992 Effect of nose bluntness on leading-edge receptivity. In *Instability, Transition and Turbulence* (ed. M. Hussaini, A. Kumar & C. Streett). Springer.
- HAMMERTON, P. W. & KERSCHEN, E. J. 1996 Boundary-layer receptivity for a parabolic leading edge. *J. Fluid Mech.* **310**, 243–267.
- HAMMERTON, P. W. & KERSCHEN, E. J. 1997 Boundary-layer receptivity for a parabolic leading edge. Part 2. The small Strouhal number limit. *J. Fluid Mech.* **353**, 205–220.
- HERBERT, T. 1991 Numerical study of leading-edge receptivity. PhD thesis, Ohio State University, Columbus, OH.
- KERSCHEN, E. J. 1990 Boundary layer receptivity theory. *Appl. Mech. Rev.* **43**, 152–157.
- LEEHEY, P., GEDNEY, C. & HER, J. 1984 The receptivity of a laminar boundary layer to external disturbances. *IUTAM Symp. on Laminar-Turbulent Transition, Novosibirsk, USSR* (ed. V. V. Kozlov). Springer.
- LIN, N., REED, H. L. & SARIC, W. S. 1991 Leading-edge receptivity: Navier–Stokes computations. In *Proc. Boundary Layer Transition and Control Conference, Cambridge, UK*.
- MORKOVIN, M. V. 1969 On the many faces of transition. *Viscous Drag Reduction*. Plenum.
- MURDOCK, J. W. 1980 The generation of a Tollmien–Schlichting wave by a sound wave. *Proc. R. Soc. Lond. A*, **372**, 517–534.
- PULLIAM, T. H. 1986 Artificial dissipation models for the Euler equation. *AIAA J.* **24**, 1931–1940.
- SARIC, W. S. & RASMUSSEN, B. K. 1992 Boundary layer receptivity: Freestream sound on an elliptic leading edge. *Bull. Am. Phys. Soc.* **37**, 1720.
- SARIC, W. S. & WHITE, E. B. 1998 Influence of high-amplitude noise on boundary-layer transition to turbulence. *AIAA Paper* 98-2645.
- SARIC, W. S., WEI, W. & RASMUSSEN, B. K. 1995 Effect of leading-edge on sound receptivity. *Laminar-Turbulent Transition*, Vol. 4. Springer.
- SHAPIRO, P. 1977 The influence of sound upon laminar boundary layer instability. *Acoustics & Vibration Lab. Rep.* 83458-83560-1, MIT.
- WANDERLEY, J. B. V. 1998 Numerical simulation of receptivity to acoustic waves on elliptic leading edges. PhD thesis, Illinois Institute of Technology.